

Article

Multiphysics Modeling of Electrochemical Impedance Spectroscopy Responses of SAM-Modified Screen-Printed Electrodes

Lara Franchin *  and Stefano Bonaldo 

Department of Information Engineering, University of Padova, 35131 Padova, Italy; stefano.bonaldo@unipd.it
* Correspondence: lara.franchin@dei.unipd.it

Abstract: In this work, we present a multiphysics modeling approach capable of simulating electrochemical impedance spectroscopy (EIS) responses of screen-printed electrodes (SPEs) modified with self-assembled monolayers of 11-Mercaptoundecanoic acid (MUA). Commercially available gold SPEs are electrochemically characterized through experimental cyclic voltammetry and EIS measurements with 10 mM $[\text{Fe}(\text{CN})_6]^{3-/4-}$ redox couple in phosphate buffered saline before and after the surface immobilization of MUA at different concentrations. We design the multiphysics model through COMSOL Multiphysics[®] based on the 3D geometry of the devices under test. The model includes four different physics considering the metal/solution interface electrochemical phenomena, the ion and electron potentials and currents, and the measurement set-up. The model is calibrated through a set of experimental measurements, allowing the tuning of the parameters used by the model. We use the calibrated model to simulate the EIS response of MUA-modified SPEs, comparing the results with experimental data. The simulations fit the experimental curves well, following the variation of MUA concentration on the surface from 1 μM to 100 μM . The EIS parameters, retrieved through a CPE-modified Randles' circuit, confirm the consistency with the experimental data. Notably, the simulated surface coverage estimates and the variation of charge transfer resistance due to MUA-immobilization are well matched with their experimental counterparts, reporting only a 2% difference and being consistent with the experimental electrochemical behavior of the SPEs.

Keywords: multiphysics model; self-assembled monolayer; screen-printed electrodes; electrochemical impedance spectroscopy



Citation: Franchin, L.; Bonaldo, S. Multiphysics Modeling of Electrochemical Impedance Spectroscopy Responses of SAM-Modified Screen-Printed Electrodes. *Sensors* **2024**, *24*, 858. <https://doi.org/10.3390/s24030858>

Received: 15 December 2023
Revised: 11 January 2024
Accepted: 25 January 2024
Published: 28 January 2024



Copyright: © 2024 by the authors. Licensee MDPI, Basel, Switzerland. This article is an open access article distributed under the terms and conditions of the Creative Commons Attribution (CC BY) license (<https://creativecommons.org/licenses/by/4.0/>).

1. Introduction

The development of electrochemical biosensors has attracted considerable interest in the last years due to their cost-effective highly-sensitive detection and their inexpensiveness [1–3]. Electrochemical biosensors are employed in a wide range of applications, e.g., smart agriculture and sustainable food production [4–8] and clinical diagnostics and smart healthcare [9–14]. For instance, the authors in [7] report an innovative biosensor based on bacterial proliferation for the timely detection of phages in milk samples, which is an important requirement for food safety in dairy production. In [13], the authors show a highly sensitive and selective biosensor for the detection of tau protein, a biomarker for early diagnosis of Alzheimer's disease. Another valuable example is reported in [14], where a flexible graphene oxide sensor with a detection limit of 0.91 μM is developed to detect the presence of H_2O_2 as the biomarker for a wide number of pathologies, such as Alzheimer's, diabetes, cancer, brain injury, and neurodegenerative disorders. The design of biosensor devices, despite proving to be powerful resources exploitable in various sectors, frequently relies on empirical assessments of their performance rather than substantial insights into their modeling before fabrication. Engineering and nanotechnology heavily rely on finite-element simulations to mathematically model physical systems. The modeling facilitates the exploration of various designs and parametric configurations within the

system, enabling the assessment of expected behavior and outcomes through alterations such as geometries, surface morphologies, properties, and testing conditions. COMSOL Multiphysics® is a commercial finite-element software which allows multiphysics simulations of non-standard geometries combining a wide range of physical phenomena, e.g., hydrodynamic and electrochemical processes [15]. The complexity of modeling the electrical responses of biosensors, like cyclic voltammetry (CV) and electrochemical impedance spectroscopy (EIS), arises from the necessity to integrate synergistic physics in the model, with appropriately calibrated parameters associated with device materials and testing conditions, employing specific equivalent circuits for signal generation and conditioning—such as potentiostat for CVs and frequency response analyzers for EISs. Finite-element simulations in COMSOL Multiphysics® can be exploited to design optimized electrodes [15–20], studying their electrochemical behavior to develop biosensors with enhanced performance. In [20], for example, an o-quinone enzymatic biosensor was modeled through COMSOL Multiphysics® and validated experimentally to study and optimize its detection capability. Despite the advantages, there are still a limited number of studies that document sensor modeling, often lacking validation through experimental measurements [16,17], seldom considering the full electrode characterization, and not thoughtfully investigating the physical, chemical, and electrical phenomena on its surface.

In this work, we present a multiphysics model capable of simulating EIS responses of electrochemical devices in the presence of surface self-assembled monolayer (SAM) functionalization. The simulations are carried out with a refined 3D multiphysics model designed with COMSOL Multiphysics® and based on screen-printed electrodes (SPEs). To ensure accurate prediction of experimental outcomes, our model undergoes meticulous calibration using a series of experimental CV and EIS measurements at different concentration levels of SAM on the surface. Subsequently, we assess the model's effectiveness by accurately simulating an additional set of EIS experimental measurements of varying surface functionalization through the immobilization of self-assembled monolayers.

2. Materials and Methods

2.1. Electrodes under Evaluation and Measurements Set-Up

The devices under evaluation were commercially available low-cost screen-printed electrodes (DRP223BT, Metrohm DropSens, Spain). These sensors were constructed with a conventional three-electrode setup, featuring gold (Au) electrodes for both the working (WE) and counter (CE) electrodes along with a silver (Ag) reference electrode (RE), all printed on a ceramic substrate measuring 34 mm × 10 mm × 0.5 mm. Figure 1a illustrates the geometrical arrangement, showcasing a central disk of 1.6-mm diameter as the WE. The electrolyte solution is placed as a 100-μL drop on top of the electrode area.

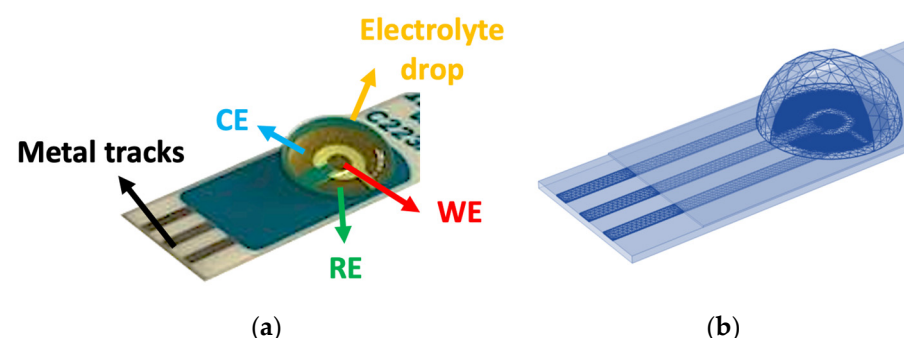


Figure 1. (a) Layout of the devices under evaluation. (b) 3D geometrical structure and mesh of the model implemented in COMSOL Multiphysics®.

For experimental characterization, the SPEs underwent analysis through cyclic voltammetry (CV) and electrochemical impedance spectroscopy (EIS) using a 100 μL solution of $\text{Fe}(\text{CN})_6^{3-}/\text{Fe}(\text{CN})_6^{4-}$ (referred as FeCN) at 10 mM of concentration in 1 × Phosphate Buffered Saline (PBS). Employing the Solartron 1260 electrochemical impedance analyzer

and the Solartron 1287 electrochemical potentiostat, CV measurements were conducted at a scan rate of 100 mV/s. For bare SPEs, the potential sweeps ranged from -0.2 V to 0.45 V, whereas for SAM-modified SPEs, they extended from -0.8 V to 0.8 V. The internal Ag electrode was used as a pseudo-reference. The redox equilibrium potential E_0 was deduced from the CV curves, yielding $E_0 = 132$ mV for bare electrodes and $E_0 = 110$ mV for SAM-modified devices. EIS measurements, carried out at $V_{DC} = E_0$ and $V_{ac} = 10$ mV, spanned a frequency range between 1 Hz and 100 kHz, using a 3-electrode configuration to characterize only WE, isolating its contributions from other electrodes [21,22]. All experimental measurements were replicated a minimum of 3 times using different devices. The EIS electric parameters were extrapolated through a modified Randles' circuit. The circuit comprises a faradaic branch, composed by a series of a charge transfer resistance (R_{ct}) and a Warburg element (W), and a parallel non-faradaic contribution where the double layer capacitance (C_{dl}) is substituted by a constant phase element (CPE). The parallel is in series with the solution/electrode resistance contribution (R_s).

2.2. Multiphysics 3D Model

The COMSOL Multiphysics® simulator operates on the finite-element method, enabling the integration of various equations governing diverse physical phenomena [23]. Our proposed model is structured in a 3D geometry, where each element possesses distinct material properties. This geometric structure comprises components like the substrate, working, counter, and reference electrodes (each 100 μm thick), metal interconnections and contact areas, an isolation layer, and the solution drop—a semi-sphere with a radius of 4.5 mm. Presently, the simulator doesn't incorporate surface roughness.

The 3D layout, involving elements like the solution drop, electrodes, and metal interconnections, is meticulously meshed using tetrahedral elements (Figure 1b). This mesh is especially refined around the interfaces of electrodes with the metal/solution, enhancing accuracy in describing electrochemical reactions. The first layer thickness of 1 μm is considered the diffusive layer, with a stretching factor of 1.1 in the volume. Simulations run within a reasonable computational timeframe—approximately 1 h for each CV curve and about 7 min for the entire frequency sweep from 100 kHz to 1 Hz for every EIS response.

The model incorporates four distinct COMSOL physics [24], enabling precise simulation of microscopic mechanisms that combine electrochemical, electrical, and chemical phenomena. These include the distribution of electrochemical species in the solution and the current exchange at the electrode/solution interface. Equations defining these processes are applied to specific elements within the 3D geometry. These equations undergo evaluation and resolution within a time-dependent transitory study. The electrochemical reaction kinetics at metal/solution interface and the electric currents and potentials applied to the electrodes and the electrolyte are modeled through the *secondary current distribution physics*. The physics is based on the extended Butler–Volmer equation where C_R and C_O are the redox species concentrations, j_0 is the exchange current density, α_c and $\alpha_a = (1 - \alpha_c)$ are redox symmetry factors, and $\eta = \Phi_s - \Phi_l - E_{eq}$ is the overpotential; where Φ_s is the electrode potential, Φ_l is the electrolyte potential, and E_{eq} is the equilibrium potential of the electrochemical cell, retrieved from E_0 using the Nernst equation for a one-electron process.

$$j = j_0 \left[C_R \exp\left(\frac{\alpha_a F \eta}{RT}\right) - C_O \exp\left(\frac{-\alpha_c F \eta}{RT}\right) \right], \quad (1)$$

The diffusive transport and the reactions of the redox couple species in the electrolyte solution are simulated through *transport of diluted species physics*, which implements the Nernst–Planck equation coupled with *secondary current distribution physics*, assuming a prevalence of diffusive mass transport. The current distributions and the electric potential on the metal tracks are modeled through *electric current physics*, based on Maxwell's classical laws, assuming negligible inductive effects. Finally, the electric signals generation, conditioning, and readouts of an ideal potentiostat are modeled through the *electric circuit module*, coupled with the metal contacts area. The ideal potentiostat is simulated through

an equivalent circuit with two operational amplifiers (gain of 10^5) which applies a linear sweep tension to control the potential between WE and RE and reads the current between WE and CE.

3. Results and Discussion

3.1. Bare SPEs Model Calibration

The proposed model is calibrated through the definition of key parameters in order to get a good fit between simulations and experimental results. The key parameters are extrapolated from a dedicated set of experimental CV and EIS measurements performed in a solution of 10 mM $\text{Fe}(\text{CN})_6^{3-}/\text{Fe}(\text{CN})_6^{4-}$ in PBS. The redox equilibrium potential E_0 is retrieved from the CV response as well as the charge transfer coefficients α_a and α_c , estimated by evaluating the symmetry of the CV curve (Figure 2).

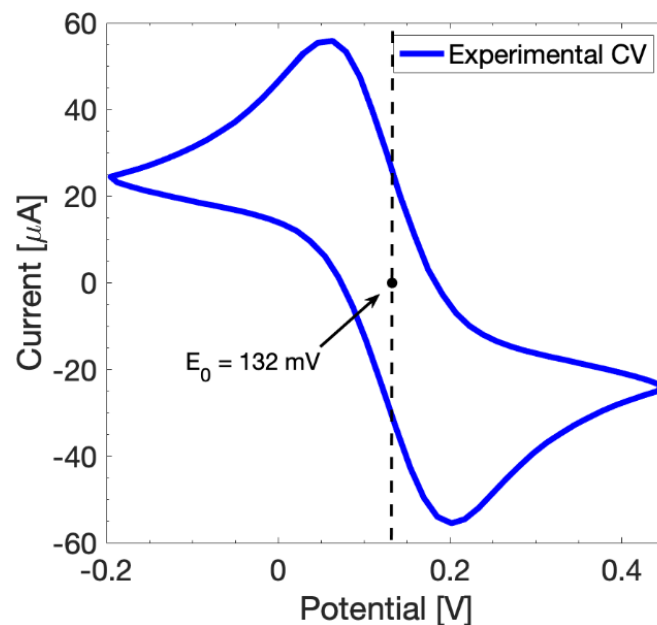


Figure 2. CV response at scan rate of 100 mV/s in a potential range from -0.2 V to 0.45 V of bare SPEs to retrieve the E_0 .

While a *CPE* could be more suitable to model the double layer of experimental electrochemical responses, to our knowledge the used software does not allow the consideration of a frequency-dependent value to model the double layer. Hence, we have estimated the double layer capacitance C_{dl} from the *CPE*. The impedance of the constant phase element (Z_{CPE}) is defined as

$$Z_{CPE} = \frac{1}{Y_0(i\omega)^n}, \quad (2)$$

where ω is angular frequency and Y_0 and n are the characteristic parameters of the *CPE*.

Since the parameter Y_0 does not have the same physical meaning as a capacitance, it is fundamental to apply a conversion method to obtain an equivalent C_{dl} value from the *CPE*. Numerous approaches have been reported in literature [25] and we choose to estimate the C_{dl} value as shown in [26]:

$$C_{dl} = Y_0(\omega''_{max})^{n-1}, \quad (3)$$

where ω''_{max} is the frequency at which the impedance imaginary part is at its maximum.

Meanwhile, the exchange charge density current j_0 is estimated from charge transfer resistance R_{ct} through (4) [27,28].

$$j_0 = \frac{RT}{nFA R_{ct}}, \quad (4)$$

Both CPE and R_{ct} values are extrapolated through fitting the EIS curve with the modified Randles' equivalent circuit. The redox species diffusion coefficients D_O and D_R are retrieved from literature [29,30], and they are considered identical, being approximated to the nearest integer. Table 1 reports the used estimated values of the key parameters.

Table 1. List of model key parameters used to calibrate the model for bare electrodes.

Parameter	Value
E_0	132 [mV]
C_{dl}	0.1 [F/m ²]
j_0	2.5 [A/m ²]
$D_R = D_O$	7×10^{-6} [cm ² /s]
α_a	0.5
α_c	0.5

After the model parameters extrapolation, we simulate the EIS responses of bare gold electrodes with COMSOL, imposing the same experimental conditions of the real measurements. The simulated curves are compared to their experimental counterparts in Figure 3. The simulated EIS Nyquist plot (Figure 3a) follows the trend of the experimental curve until the Warburg branch, where the diffusivity and other non-modellable slow processes start to influence the experimental measurements. Overall, the model is able to predict the EIS measurements quite well. The EIS parameters are extrapolated through the CPE-modified Randles' circuit reported as an inset in Figure 3a. The simulated R_{ct} value is only less than 15% different from the experimental value. The Bode magnitude diagram (Figure 3b, top plot) evidences a slight increase of the simulated R_s with respect to the experimental value (+27.5%). This difference can be attributed to the experimental error since the simulator accounts for ideal conditions. Meanwhile, the Bode phase plot (Figure 3b, bottom) shows as phase displacement of the simulated curve due to shift at an intermediate frequency around 2 kHz. It is worth noting that COMSOL does not allow the simulation of a constant phase element and accounts only for double layer capacitance. The C_{dl} value used in the simulation needs to be estimated from CPE with (3), as previously reported, partially affecting the accuracy of the model estimate. In addition, the simulated curve can be fitted with the equivalent electric circuit with a CPE parameter n equal to 1, demonstrating that the model implements an ideal capacitance as the double layer. On the other hand, the experimental data show $n = 0.91$, evidencing that, experimentally, the double layer should be considered as almost-ideal capacitance. These considerations are most likely the cause of frequency shift visible in Figure 3b at low-intermediate frequencies.

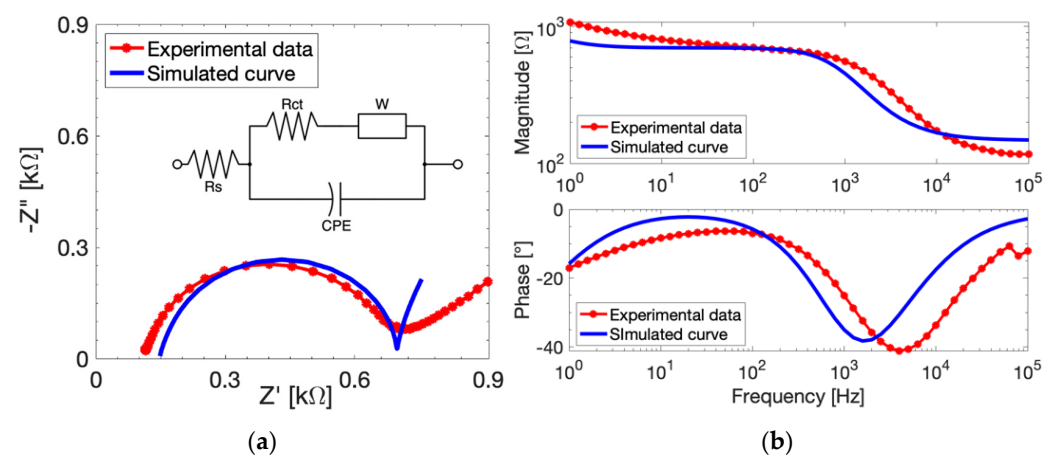


Figure 3. Experimental (red dotted curves) and simulated (blue curves) electrochemical responses of bare electrodes measured with 10 mM FeCN in PBS. (a) EIS Nyquist diagram at $V_{DC} = 132$ mV and $V_{AC} = 10$ mV, with CPE-modified equivalent circuit as inset. (b) Magnitude (top) and phase (bottom) of EIS responses at $V_{DC} = 132$ mV and $V_{ac} = 10$ mV.

3.2. SAM-Modified SPEs Model Calibration

We functionalize the SPEs' surface with a SAM of 11-Mercaptoundecanoic acid (MUA). We selected MUA due to its strong binding with gold surfaces and the stability of its monolayer. In addition, MUA is widely used for surface passivation before immobilizing specific recognition elements such as proteins and antibodies [31,32]. The electrodes are soaked in an ethanolic solution at different concentrations of MUA in a range from 1 μM to 100 μM for 1 h to allow for the SAM's immobilization. The time of functionalization and the concentration range are retrieved from well-consolidated immobilization procedures reported in the literature [32]. We carefully rinsed the devices with bi-distilled water and then perform electrochemical characterizations through CV and EIS measurements with a concentration of 10 mM FeCN in PBS. We take as reference the CV and EIS measurements with SPEs functionalized with MUA at a concentration of 1 μM to report the calibration results.

To simulate the electrochemical response of MUA-modified SPEs, we need to take into account the SAM surface modification in the proposed model. The molecular immobilization can be modeled through a variation of the exchange current density j_0 , caused by the change in the electron transfer capabilities due to the surface modification, which reflects on the parameter [33,34]. Hence, the exchange current density j_0 at each considered MUA concentration is calculated once again through (2) by extrapolating the R_{ct} values from experimental EIS curves. The redox equilibrium potential E_0 is retrieved from the CV response as well as the charge transfer coefficients α_a and α_c , estimated by evaluating the symmetry of the CV curve (Figure 4). In this case, the retrieved value of E_0 is 110 mV, while the current peaks present a slight asymmetry since the anodic and cathodic peaks ratio is 0.8. Therefore, the symmetry coefficients are adjusted accordingly. C_{dl} , D_{ox} , and D_{red} are retrieved as reported in Section 3.1. The values used for the calibration of the 1 μM -MUA-modified SPEs simulation are reported in Table 2.

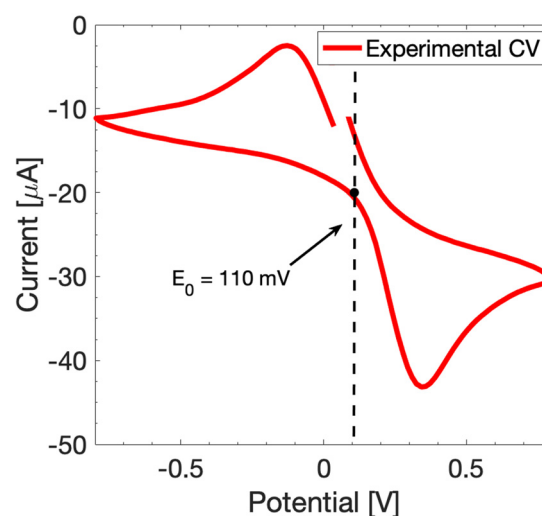


Figure 4. CV response at scan rate of 100 mV/s in a potential range from -0.8 V to 0.8 V of 1 μM -MUA-modified SPEs to retrieve the E_0 .

Table 2. List of parameters used to calibrate the model for SAM-modified electrodes.

Parameter	Value
E_0	110 [mV]
C_{dl}	0.1 [F/m ²]
j_0	0.55 [A/m ²]
$D_{red} = D_o$	7.1×10^{-6} [cm/s]
α_a	0.6
α_c	0.4

After the parameters' extrapolation, we simulated the EIS responses of MUA-modified gold electrodes with COMSOL imposing the same experimental conditions of the real measurements. The simulated and the experimental EIS signals of 1 μM -MUA-modified SPEs are compared in Figure 5. The experimental EIS Nyquist plot (Figure 5a) is well-matched with the simulated curve, reporting only a slight difference at the Warburg branch, characterized by slow diffusive processes at lower frequencies which are highly affected by experimental error. The R_{ct} values are extrapolated with the CPE-modified Randles' circuit, and they differ only by 7%. The simulated R_s is 40- Ω higher with respect to the experimental value, which is evident in the Bode magnitude diagram (Figure 5b, top plot). This difference between the simulation and the experimental behavior is possibly caused by a non-homogenous functionalization of the surface due to non-ideality of the real device. Moreover, the Bode phase plot (Figure 5b, bottom) reports a displacement at the high-intermediate frequencies shown—similar to the bare electrodes—which is once again probably due to the double layer capacitance. An interesting aspect is that the frequency shift in Figure 5b is not as evident as Figure 3b. This is probably due to the surface functionalization. In this case, the experimental CPE parameter n is equal to 0.95, which is higher than the bare electrode n value, suggesting that the experimental double layer may be closer to an ideal capacitance in the presence of surface functionalization.

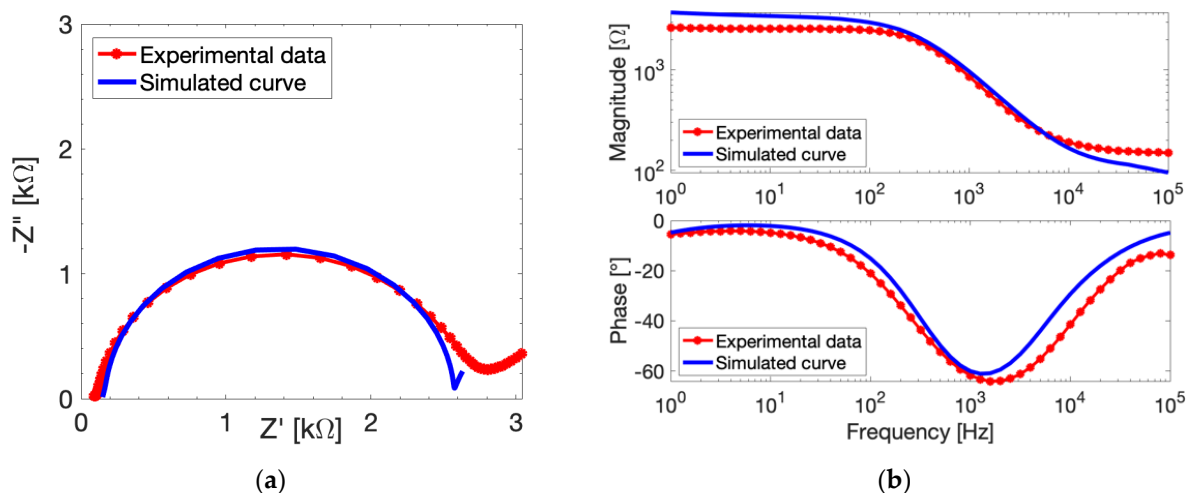


Figure 5. Experimental (red dotted curves) and simulated (blue curves) electrochemical responses of 1 μM -MUA-modified SPEs measured with 10 mM FeCN in PBS. (a) EIS Nyquist diagram at $V_{DC} = 132$ mV and $V_{AC} = 10$ mV. (b) Magnitude (top) and phase (bottom) of EIS responses at $V_{DC} = 132$ mV and $V_{ac} = 10$ mV.

After model calibration, we simulate a new data set of experimental measurements at different MUA concentrations, aiming to demonstrate the model's predictive capability of EIS response for SAM-modified SPEs with different levels of surface functionalization. In this case, all the model parameters are kept fixed except for j_0 , which is adjusted according to the MUA concentration used for the functionalization. Figure 6 reports the comparison between the simulations and the Nyquist plots of the experimental EIS measurements with different MUA concentrations. All the simulated curves fit their experimental counterparts well from high frequencies to medium-low frequencies (100 kHz to 100 Hz) and are able to follow the increase of MUA functionalization on the surface with the same considerations as discussed above. In particular, the simulated R_{ct} are well matched with the experimental values, e.g., for an MUA concentration of 50 μM the variation between simulated and experimental R_{ct} is less than 5%. Therefore, it can be concluded that the proposed model is capable of simulating EIS responses of SPEs accounting for MUA presence at different concentrations.

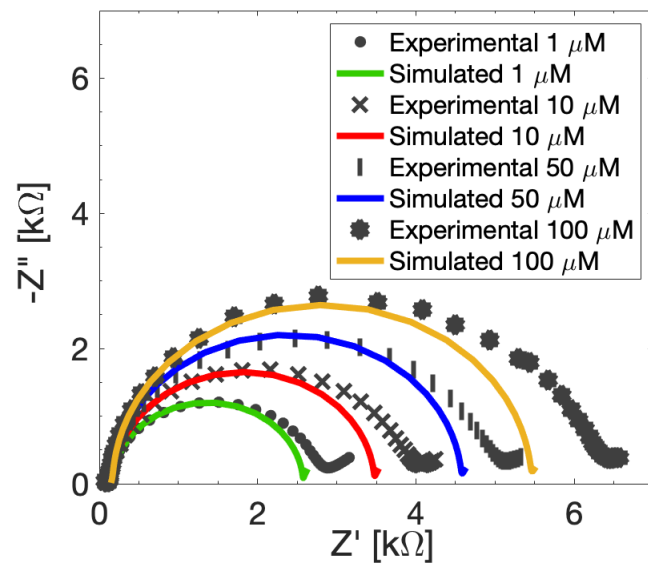


Figure 6. Experimental (red dotted curves) and simulated (blue curves) EIS Nyquist diagram of the electrochemical responses of modified SPEs at different MUA concentrations measured with 10 mM FeCN in PBS, at $V_{DC} = 132$ mV and $V_{AC} = 10$ mV.

3.3. Assessment of Simulated Surface Coverage and Variation of Charge Transfer Resistance

In electrochemical biosensing applications, the variation of the charge transfer resistance is often a crucial parameter to determine whether a surface modification has occurred correctly or if the device under examination can detect the analytes of interest. Having a model capable of simulating this behavior can be helpful for sensor design and development before actual device fabrication. Hence, in this section we evaluate how the proposed model can predict the experimental variation of charge transfer resistance due to the surface functionalization. First, we calculate the level of the molecular immobilization on the electrode by calculating the surface coverage θ using (4) through the R_{ct} values of bare electrodes and MUA-functionalized devices, extrapolated from EIS experimental measurements [35].

$$\theta = 1 - \frac{R_{ct_bare}}{R_{ct_MUA}} \quad (5)$$

The comparison between the simulated and experimental θ is reported in Figure 7a. It is evident that the simulated data follow the same trend as the experimental values, and the reported coverage only differs by <2% for all the MUA concentrations. Hence, simulated surface coverage is very similar to the experimental θ . The percentual variation of the charge transfer resistance (ΔR_{ct}) between MUA-modified sensors and their bare measurements is evaluated in Figure 7b. All the simulated ΔR_{ct} show a good match with the experimental average values, being well within the reported experimental error for all the MUA-concentrations. These results clearly demonstrate the model capability to predict the electrochemical response of SPEs devices after surface functionalization with MUA, suggesting that the proposed model may also be a reliable tool for simulating electrochemical detection of other surface-immobilized molecules such as DNA and proteins.

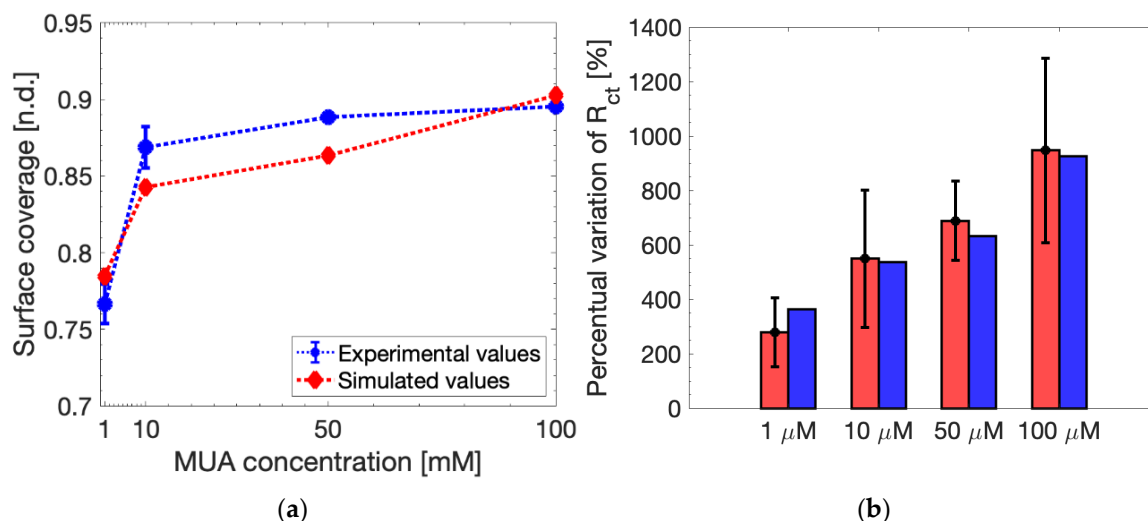


Figure 7. (a) Simulated surface coverage compared to the experimental data. (b) Simulated R_{ct} variation to the experimental data measured at $V_{DC} = 132$ mV and $V_{ac} = 10$ mV.

4. Conclusions

In this work, we propose a multiphysics model to simulate the electrochemical responses of MUA-functionalized commercial screen-printed biosensors. The model requires a careful calibration through dedicated tests with CV and EIS measurements. The model is validated by simulating a new set of EIS curves at different MUA concentrations. Our model has proven to be a reliable tool for the simulation and prediction of the electrochemical behavior of biosensing systems with surface molecular immobilization, being useful for simulating the electrochemical response of functionalized screen-printed electrodes, which may aid the development and design of biosensors before device fabrication. Simulated curves of MUA-modified electrodes fit the experimental data well, with simulated $R_{ct} < 7\%$ different from the experimental values. The variation of R_{ct} due to MUA surface immobilization at different concentrations reports values well within the experimental error, and the simulated surface coverage is only 2% less than the experimental values. These promising results suggest that the model can be exploited to simulate a wide range of biosensing applications, including more complex surface functionalization. In the future, we plan to further test the model considering DNA immobilization and protein presence on the surface device.

Author Contributions: Conceptualization, L.F. and S.B.; methodology, L.F.; software, L.F. and S.B.; validation, L.F.; formal analysis, L.F.; investigation, L.F.; resources, S.B.; data curation, L.F.; writing—original draft preparation, L.F.; writing—review and editing, L.F. and S.B.; visualization, L.F.; supervision, S.B.; project administration, S.B.; funding acquisition, S.B. All authors have read and agreed to the published version of the manuscript.

Funding: This research received no external funding.

Institutional Review Board Statement: Not applicable.

Informed Consent Statement: Not applicable.

Data Availability Statement: Data are contained within the article.

Conflicts of Interest: The authors declare no conflicts of interest.

References

- Grieshaber, D.; MacKenzie, R.; Vörös, J.; Reimhult, E. Electrochemical Biosensors—Sensor Principles and Architectures. *Sensors* **2008**, *8*, 1400–1458. [[CrossRef](#)]
- Kerman, K.; Kobayashi, M.; Tamiya, E. Recent Trends in Electrochemical DNA Biosensor Technology. *Meas. Sci. Technol.* **2004**, *15*, R1–R11. [[CrossRef](#)]

3. Sadeghi, M.; Kashanian, S.; Naghib, S.M.; Arkan, E. A High-Performance Electrochemical Aptasensor Based on Graphene-Decorated Rhodium Nanoparticles to Detect HER2-ECD Oncomarker in Liquid Biopsy. *Sci. Rep.* **2022**, *12*, 3299. [CrossRef]
4. Alexandre, D.L.; Melo, A.M.A.; Furtado, R.F.; Borges, M.F.; Figueiredo, E.A.T.; Biswas, A.; Cheng, H.N.; Alves, C.R. A Rapid and Specific Biosensor for *Salmonella* Typhimurium Detection in Milk. *Food Bioprocess Technol.* **2018**, *11*, 748–756. [CrossRef]
5. Rosati, G.; Ravarotto, M.; Scaramuzza, M.; De Toni, A.; Paccagnella, A. Silver Nanoparticles Inkjet-Printed Flexible Biosensor for Rapid Label-Free Antibiotic Detection in Milk. *Sens. Actuators B Chem.* **2019**, *280*, 280–289. [CrossRef]
6. Bonaldo, S.; Franchin, L.; Pasqualotto, E.; Cretaio, E.; Losasso, C.; Peruzzo, A.; Paccagnella, A. Influence of BSA Protein on Electrochemical Response of Genosensors. *IEEE Sens. J.* **2023**, *23*, 1786–1794. [CrossRef]
7. Bonaldo, S.; Franchin, L.; Cretaio, E.; Pasqualotto, E.; Scaramuzza, M.; Paccagnella, A. Electrochemical Biosensor for the Monitoring of Phages of *Lactococcus lactis* in Milk-Based Samples. *IEEE Sens. J.* **2024**, *24*, 78–85. [CrossRef]
8. Yang, Z.; Zhang, X.; Guo, J. Functionalized Carbon-Based Electrochemical Sensors for Food and Alcoholic Beverage Safety. *Appl. Sci.* **2022**, *12*, 9082. [CrossRef]
9. Sadeghi, M.; Kashanian, S.; Naghib, S.M.; Askari, E.; Haghirsadat, F.; Tofighi, D. A Highly Sensitive Nanobiosensor Based on Aptamer-Conjugated Graphene-Decorated Rhodium Nanoparticles for Detection of HER2-Positive Circulating Tumor Cells. *Nanotechnol. Rev.* **2022**, *11*, 793–810. [CrossRef]
10. Hasan, M.R.; Ahommed, M.S.; Daizy, M.; Bacchu, M.S.; Ali, M.R.; Al-Mamun, M.R.; Saad Aly, M.A.; Khan, M.Z.H.; Hossain, S.I. Recent Development in Electrochemical Biosensors for Cancer Biomarkers Detection. *Biosens. Bioelectron. X* **2021**, *8*, 100075. [CrossRef]
11. Parnianchi, F.; Kashanian, S.; Nazari, M.; Peacock, M.; Omidfar, K.; Varmira, K. Ultrasensitive Electrochemical Sensor Based on Molecular Imprinted Polymer and Ferromagnetic Nanocomposite for Bilirubin Analysis in the Saliva and Serum of Newborns. *Microchem. J.* **2022**, *179*, 107474. [CrossRef]
12. Rosati, G.; Urban, M.; Zhao, L.; Yang, Q.; de Carvalho Castro e Silva, C.; Bonaldo, S.; Parolo, C.; Nguyen, E.P.; Ortega, G.; Fornasiero, P.; et al. A Plug, Print & Play Inkjet Printing and Impedance-Based Biosensing Technology Operating through a Smartphone for Clinical Diagnostics. *Biosens. Bioelectron.* **2022**, *196*, 113737. [CrossRef]
13. Ben Hassine, A.; Raouafi, N.; Moreira, F.T.C. Novel Biomimetic Prussian Blue Nanocubes-Based Biosensor for Tau-441 Protein Detection. *J. Pharm. Biomed. Anal.* **2023**, *226*, 115251. [CrossRef] [PubMed]
14. Erçarıkcı, E.; Dağcı Kıranşan, K.; Topçu, E. A Flexible Graphene Paper Electrochemical Sensor with Electrodeposited Ag and Ni Nanoparticles for H₂O₂ Detection. *IEEE Sens. J.* **2023**, *23*, 7087–7094. [CrossRef]
15. Dickinson, E.J.F.; Ekström, H.; Fontes, E. COMSOL Multiphysics®: Finite Element Software for Electrochemical Analysis. A Mini-Review. *Electrochem. Commun.* **2014**, *40*, 71–74. [CrossRef]
16. Zainuddin, A.A.; Nordin, A.N.; Rahim, R.A.; Mak, W.C. Modeling of a Novel Biosensor with Integrated Mass and Electrochemical Sensing Capabilities. In Proceedings of the 2016 IEEE EMBS Conference on Biomedical Engineering and Sciences (IECBES), Kuala Lumpur, Malaysia, 4–8 December 2016; pp. 420–425.
17. Farhana Roslan, N.A.; Rahim, R.A.; Md Ralib, A.A.; Za'bah, N.F.; Nordin, A.N.; Riza Bashri, M.S.; Suhaimi, M.I.; Samsudin, Z.; Ming, L.L.; Sugandi, G. Simulation of Geometrical Parameters of Screen Printed Electrode (SPE) for Electrochemical-Based Sensor. In Proceedings of the 2021 IEEE Regional Symposium on Micro and Nanoelectronics (RSM), Kuala Lumpur, Malaysia, 2–4 August 2021; pp. 137–140.
18. Abdallah, M. Design, Simulation, and Development of a BioSensor for Viruses Detection Using FPGA. *IEEE J. Transl. Eng. Health Med.* **2021**, *9*, 1–6. [CrossRef]
19. Bharathi, S.J.; Thilagar, S.H.; Jayasurya, V. Design and Modeling of Electrochemical Sensor for Determining ION Concentration. In Proceedings of the 2019 IEEE 1st International Conference on Energy, Systems and Information Processing (ICESIP), Chennai, India, 4–6 July 2019; pp. 1–5.
20. Kaffash, A.; Rostami, K.; Zare, H.R. Modeling of an Electrochemical Nanobiosensor in COMSOL Multiphysics to Determine Phenol in the Presence of Horseradish Peroxidase Enzyme. *Enzyme Microb. Technol.* **2019**, *121*, 23–28. [CrossRef]
21. Grossi, M.; Riccò, B. Electrical Impedance Spectroscopy (EIS) for Biological Analysis and Food Characterization: A Review. *J. Sens. Syst.* **2017**, *6*, 303–325. [CrossRef]
22. Lisdat, F.; Schäfer, D. The Use of Electrochemical Impedance Spectroscopy for Biosensing. *Anal. Bioanal. Chem.* **2008**, *391*, 1555–1567. [CrossRef]
23. COMSOL Multiphysics® Software—Understand, Predict, and Optimize®. Available online: <https://www.comsol.com/comsol-multiphysics> (accessed on 10 December 2023).
24. Bonaldo, S.; Franchin, L.; Rosati, G.; Tonello, S.; Merkoçi, A.; Paccagnella, A. Multiphysics Simulations of Screen-Printed Electrodes for Electrochemical Biosensing. In Proceedings of the 2023 IEEE International Workshop on Metrology for Industry 4.0 & IoT (MetroInd4.0&IoT), Brescia, Italy, 6 June 2023; pp. 320–325.
25. Chang, B.-Y. Conversion of a Constant Phase Element to an Equivalent Capacitor. *J. Electrochem. Sci. Technol.* **2020**, *11*, 318–321. [CrossRef]
26. Hsu, C.H.; Mansfeld, F. Technical Note: Concerning the Conversion of the Constant Phase Element Parameter Y_0 into a Capacitance. *Corrosion* **2001**, *57*, 747–748. [CrossRef]
27. Swamy, T.; Chiang, Y.-M. Electrochemical Charge Transfer Reaction Kinetics at the Silicon-Liquid Electrolyte Interface. *J. Electrochem. Soc.* **2015**, *162*, A7129–A7134. [CrossRef]

28. Krishnaveni, P.; Ganesh, V. Electron Transfer Studies of a Conventional Redox Probe in Human Sweat and Saliva Bio-Mimicking Conditions. *Sci. Rep.* **2021**, *11*, 7663. [[CrossRef](#)] [[PubMed](#)]
29. Konopka, S.J.; McDuffie, B. Diffusion Coefficients of Ferri- and Ferrocyanide Ions in Aqueous Media, Using Twin-Electrode Thin-Layer Electrochemistry. *Anal. Chem.* **1970**, *42*, 1741–1746. [[CrossRef](#)]
30. Saraç, H.; Patrick, M.A.; Wragg, A.A. Physical Properties of the Ternary Electrolyte Potassium Ferri-Ferrocyanide in Aqueous Sodium Hydroxide Solution in the Range 10–90 °C. *J. Appl. Electrochem.* **1993**, *23*, 51–55. [[CrossRef](#)]
31. Caglayan, M.O. Plasmon Resonance-Enhanced Internal Reflection Ellipsometry for the Trace Detection of Mercuric Ion. *Int. J. Environ. Sci. Technol.* **2018**, *15*, 909–914. [[CrossRef](#)]
32. Aizawa, H.; Gokita, Y.; Park, J.-W.; Yoshimi, Y.; Kurosawa, S. Antibody Immobilization on Functional Monolayers Using a Quartz Crystal Microbalance. *IEEE Sens. J.* **2006**, *6*, 1052–1056. [[CrossRef](#)]
33. Eckermann, A.L.; Feld, D.J.; Shaw, J.A.; Meade, T.J. Electrochemistry of Redox-Active Self-Assembled Monolayers. *Coord. Chem. Rev.* **2010**, *254*, 1769–1802. [[CrossRef](#)]
34. Liu, B.; Bard, A.J.; Li, C.-Z.; Kraatz, H.-B. Scanning Electrochemical Microscopy. 51. Studies of Self-Assembled Monolayers of DNA in the Absence and Presence of Metal Ions. *J. Phys. Chem. B* **2005**, *109*, 5193–5198. [[CrossRef](#)]
35. Sánchez-Pomales, G.; Santiago-Rodríguez, L.; Rivera-Vélez, N.E.; Cabrera, C.R. Control of DNA Self-Assembled Monolayers Surface Coverage by Electrochemical Desorption. *J. Electroanal. Chem.* **2007**, *611*, 80–86. [[CrossRef](#)]

Disclaimer/Publisher’s Note: The statements, opinions and data contained in all publications are solely those of the individual author(s) and contributor(s) and not of MDPI and/or the editor(s). MDPI and/or the editor(s) disclaim responsibility for any injury to people or property resulting from any ideas, methods, instructions or products referred to in the content.